Exchange control in a MOS double quantum dot made using a 300 mm wafer process

Jacob F. Chittock-Wood,[1,2,*] Ross C. C. Leon,[1] Michael A. Fogarty,[1] Tara Murphy,[1,3] Sofia M. Patomäki,[1,2]
Giovanni A. Oakes,[1] Felix-Ekkehard von Horstig,[1,3] Nathan Johnson,[2] Julien Jussot,[4] Stefan Kubicek,[4]
Bogdan Govoreanu,[4] David F. Wise,[1] M. Fernando Gonzalez-Zalba,[1,†] and John J. L. Morton[1,2,‡]

[1] *Quantum Motion, 9 Sterling Way, London N7 9HJ, United Kingdom*
[2] *London Centre for Nanotechnology, UCL, London WC1H 0AH, United Kingdom*
[3] *Department of Materials Sciences and Metallurgy, University of
Cambridge, Charles Babbage Rd, Cambridge CB3 0FS, United Kingdom*
[4] *IMEC, Kapeldreef 75, 3001 Leuven, Belgium*
(Dated: August 5, 2024)

Leveraging the advanced manufacturing capabilities of the semiconductor industry promises to help scale up silicon-based quantum processors by increasing yield, uniformity and integration. Recent studies of quantum dots fabricated on 300 mm wafer metal-oxide-semiconductor (MOS) processes have shown control and readout of individual spin qubits, yet quantum processors require two-qubit interactions to operate. Here, we use a 300 mm wafer MOS process customized for spin qubits and demonstrate coherent control of two electron spins using the spin-spin exchange interaction, forming the basis of an entangling gate such as $\sqrt{\text{SWAP}}$. We observe gate dephasing times of up to $T_2^* \approx 500$ ns and a gate quality factor of 10. We further extend the coherence by up to an order of magnitude using an echo sequence. For readout, we introduce a dispersive readout technique, the radiofrequency electron cascade, that amplifies the signal while retaining the spin-projective nature of dispersive measurements. Our results demonstrate an industrial grade platform for two-qubit operations, alongside integration with dispersive sensing techniques.

Silicon-based quantum processors have been recently shown to satisfy the requirements for fault-tolerant quantum computing in small systems of up to 2 qubits. Such requirements include qubit initialisation, control, and measurement fidelity above the thresholds required to implement quantum error correcting codes [1–6]. For electron spin qubits in quantum dots (QDs), further progress has been demonstrated, such as simple instances of error correction in a 3-qubit device [7] and operation of a 6-qubit processor [8] indicating that the technology is ready to be scaled up. To that purpose, it is timely to begin leveraging the manufacturing benefits of the semiconductor industry [9]. This approach promises to produce arrays of qubits with high-yield and reproducibility [10] while facilitating the integration with classical electronics into an integrated quantum computing system [11, 12].

There are several ways to form spin qubits within silicon devices [13, 14], however, those based on metal-oxide-semiconductor (MOS) QDs are of particular interest for industrial manufacturing due to their similarities with silicon field-effect transistors (FETs). As for modern FETs, such QDs can be formed in planar MOS devices [15], or within etched silicon nanowires [16]. The ability to form and operate high quality qubits within silicon MOS structures has been well established [14, 17, 18], motivating recent demonstrations of single qubit performance in MOS devices fabricated using semiconductor manufacturing lines [16, 19]. In this Article, we study electron spins within a silicon double quantum dot (DQD) device

fabricated using a 300mm wafer line [10, 20]. We present two key results: First, we introduce a new in-situ dispersive sensing mechanism (termed *radiofrequency- electron cascade*) with enhanced sensitivity for spin qubit readout. Second, we demonstrate control of an exchange-mediated coherent interaction, which forms the basis for a $\sqrt{\text{SWAP}}$ gate between two spin qubits. To achieve the latter, we characterise the angular dependence of the Rashba and Dresselhaus spin-orbit fields to find the optimal in-plane magnetic field direction for operation. We then characterise the exchange interaction as a function of the detuning between the two QDs, and study the effect of an 'echo' sequence [21] to mitigate the impact of low-frequency charge noise.

RADIOFREQUENCY ELECTRON CASCADE READOUT

Reading out spin qubits within semiconductor QDs typically involves mapping a spin state of interest onto a charge state of one or more QDs [22, 23], which can then be detected using a variety of charge sensing methods [24]. For example, Pauli spin blockade (PSB) can be used to map the singlet and triplet states of a pair of spin qubits onto two different charge configurations of a DQD (e.g. (1,1) or (0,2)), which are then detected by a single electron transistor [25] or single electron box [26]. *In-situ* dispersive readout of a DQD combines these into a single step, using PSB to directly distinguish between singlet and triplet states through their difference in AC polarisability [27]. This difference in polarisability is detected by incorporating the DQD into a radiofrequency (rf) tank circuit and measuring changes in the reflected rf signal.

* jacob.chittock-wood.15@ucl.ac.uk
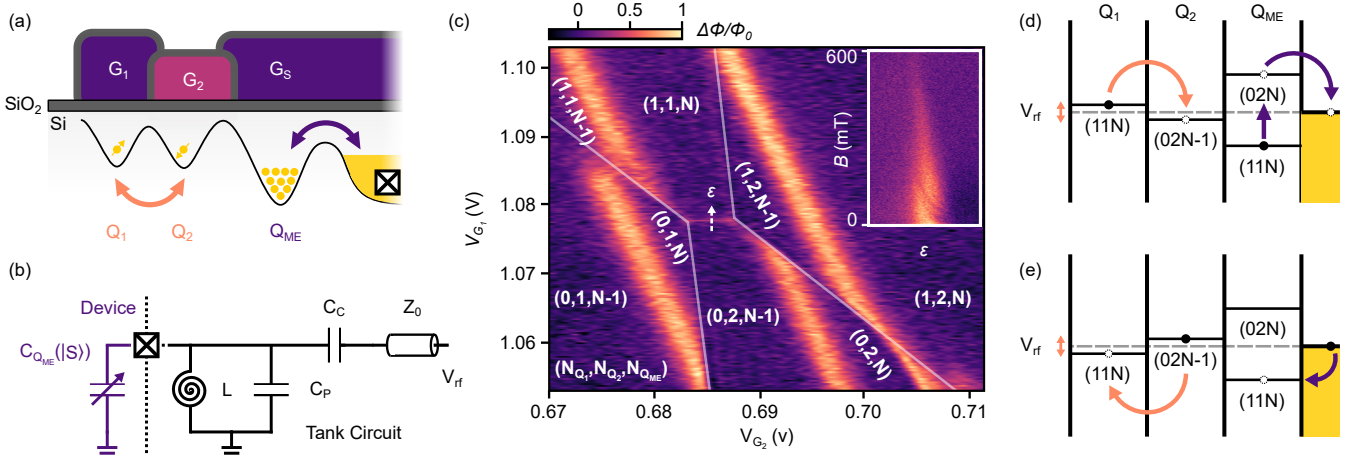† fernando@quantummotion.tech
‡ john@quantummotion.tech

FIG. 1. | **Radio-frequency driven electron cascade**. **a**, Cross-section schematic of the quantum dot array. Gates G_1 and G_2 define QDs, Q_1 and Q_2, tuned to the two-electron occupancy. The DQD is capacitively coupled to dot Q_{ME} occupied with many electrons and is controlled by gate G_S. Arrows indicate single electron tunnelling events. **b** Schematic of the rf resonator bonded to the reservoir contact of the device, including a circuit equivalent representation of the QD array as a spin dependent variable capacitor $C_{Q_{ME}}(|S\rangle)$. The resonator is formed by an off-chip superconducting spiral inductor arranged in parallel with the parasitic capacitance C_P of the assembly. **c**, Charge stability diagram of the DQD. Inset: magneto-spectroscopy of the interdot charge transition of the DQD along detuning, ε **d-e**, Schematic representations of the cascade process in which the rf excitation synchronously drives charge transitions within the QD array. **d**, A change in the charge configuration of the DQD from $(1,1)$ to $(0,2)$ raises the electrochemical potential of the Q_{ME} above the Fermi level, causing one electron to synchronously escape to the reservoir. **e**, When the DQD is driven back to $(1,1)$, an electron tunnels back from the reservoir to Q_{ME}.

However, *in-situ* dispersive readout has suffered from low sensitivity in planar MOS silicon quantum devices due to the relatively low gate lever arms [28]. To improve the sensitivity of this technique, we introduce a third quantum dot (QD) coupled to a charge reservoir, which acts as an amplifier in measuring the AC-polarisability of the DQD. Instead of measuring the usual single-electron alternating current generated by the cyclic tunneling between the two-spin singlet states of the DQD [24], we leverage the *synchronised* single-electron AC current at the third dot-reservoir system generated as a consequence of the strong capacitive coupling to the DQD. Such an approach offers the benefit of charge enhancement techniques such as latching [29], dc cascading [30] and spin-polarized single-electron boxes [31] while retaining the non-demolition nature of *in-situ* dispersive readout methods [32].

We use a device based on planar silicon MOS technology with an overlapping gate design (see Fig 1(a)). Quantum dots Q_1 and Q_2 form a DQD which we tune to hold two electrons, while Q_2 is capacitively coupled to a multi-electron quantum dot (Q_{ME}) that can exchange electrons with a charge reservoir. To measure the charge state of the system, we connect a superconducting spiral inductor to the reservoir forming an *LC* resonator (see Fig. 1(b)). At voltages where the charge in Q_{ME} is bistable, cyclic tunneling generated by the small rf signal supplied to the resonator produces a change in capacitance that can be detected as a change in the phase response, $\Delta\Phi$, using homodyne techniques [24]. Lines in gate voltage space showing Q_{ME} charge bistability are

shifted when intersecting charge transitions of the DQD, as shown in Fig. 1(c). Such shifts form the basis of dispersive charge sensing measurements [26, 34, 35] which we do not exploit here. Instead, we focus on the directly observable AC signal in the region of gate voltage space where charge transitions may occur between Q_1 and Q_2. We ascribe this signal to a two-electron charge cascade effect driven by the rf excitation, which we explain using the diagrams in Fig. 1(d-e). Consider an rf cycle in which the system starts in the occupation configuration $(N_{Q_1}, N_{Q_2}, N_{Q_{ME}}) = (1, 1, N)$. Due to the strong capacitive coupling between Q_2 and Q_{ME}, the rf excitation that drives the DQD from the $(1,1)$ to $(0,2)$ state synchronously forces an electron out of Q_{ME} in a cascaded manner, leading to $(0, 2, N-1)$. The second half of the rf cycle then reverses the process. Overall, the rf cascade measures the polarizability of the DQD system, as for *in-situ* dispersive readout measurements [28, 36], but with the substantial advantage that the induced charge can be much greater, resulting in a dispersive measurement with greater sensitivity (see App. A for more discussion on the requirements for rf electron cascade readout). Specifically, we find the voltage signal is amplified in the cascade approach compared to direct dispersive readout, by a factor

$$A = 1 + \frac{1 - \alpha_{r,ME}}{\alpha_{r,2} - \alpha_{r,1}} > 1, \tag{1}$$

where $\alpha_{r,j}$ represents the gate lever arm between the reservoir and QD j. Particularly, the sensor detects not only the interdot gate polarization charge $(\alpha_{r,1} - \alpha_{r,2})e$
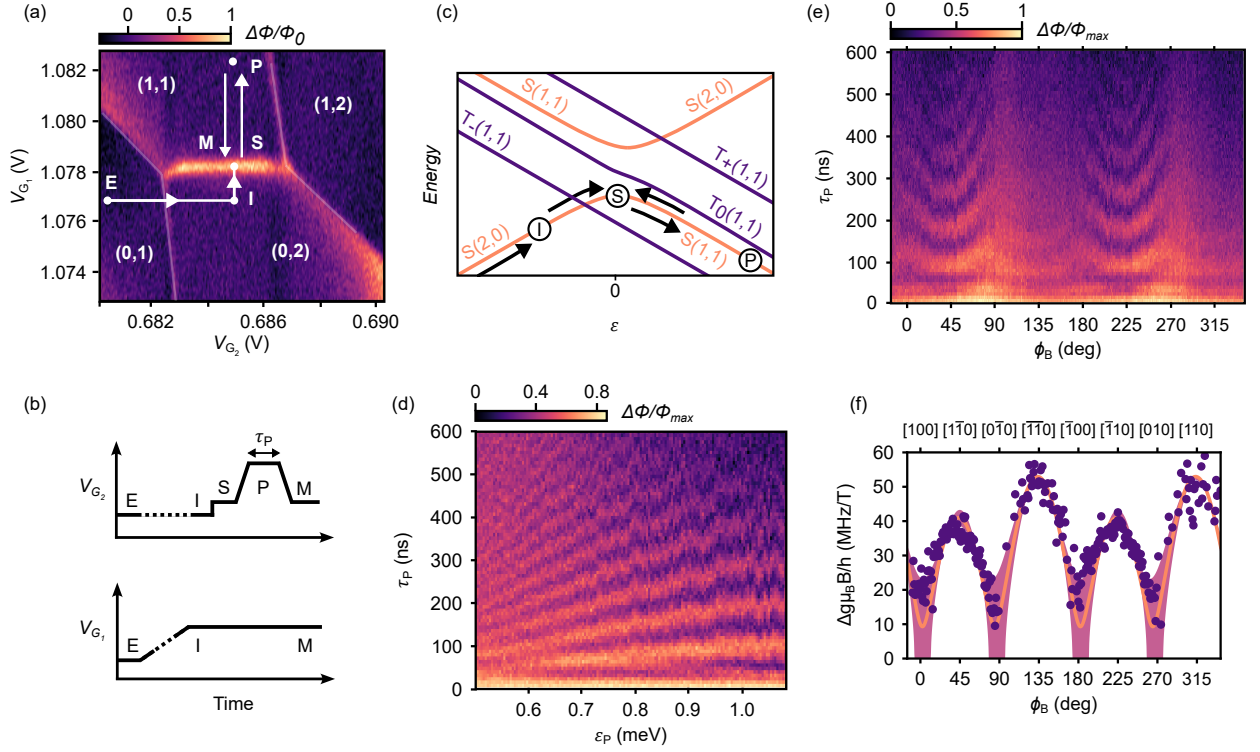
FIG. 2. | **Measurement of the spin-orbit interaction**. **a**, Charge stability diagram of the DQD around the (1,1)-(0,2) charge transition with voltage pulse sequence overlaid (shown also as a function of time in panel **b**, where dashed lines indicate longer durations). **c**, Energy diagram showing dependence of the two-electron spin states, singlet $|S\rangle$ and triplet $|T\rangle$ as a function of detuning ε. **d**, $|S\rangle$-$|T_0\rangle$ oscillations as a function of duration τ_P and detuning at point P ϵ_P in the pulse sequence ($B = 250$ mT, $\phi_B = 235°$). **e,f**, $|S\rangle$-$|T_0\rangle$ oscillation frequency dependence as a function of the in-plane magnetic field orientation ϕ_B, measured at fixed detuning $\varepsilon_P = 0.926$ meV. The fit in **f** is obtained using the spin-orbit interaction model described in Eq. (2) and incorporates the error in σ_{HF} and $J(\varepsilon_P)$.

but also the cascaded charge collected at the reservoir, $(1 - \alpha_{\mathrm{r,ME}})e$, (see App. B). We highlight that, as opposed to other charge enhancement techniques [29–31], the rf electron cascade retains the non-demolition nature of *in-situ* dispersive readout measurements since the DQD system remains in an eigenstate after a measurement is performed [37, 38].

We use the rf-cascade to distinguish the singlet and triplet states of the DQD via PSB. The signature of PSB can be observed by measuring the asymmetric disappearance of the interdot charge transitions as a function of increasing applied magnetic field [27], as shown in the inset to Fig. 1(c). At low magnetic field, the system is free to oscillate between singlet states ($|S(1,1)\rangle \leftrightarrow |S(0,2)\rangle$) due to the action of the rf drive, yielding a signal in the rf response. At high fields, however, the separated triplet $|T_-(1,1)\rangle$ state becomes the ground state for all relevant values of detuning, preventing a charge transition and resulting in the disappearance of the signal, initially for the region of the transition closer to the (1,1) charge configuration. A quantum capacitance-based simulation of the data in the inset suggests an inter-dot tunnel coupling of $t_c = 2.4$ GHz and electron temperature $T_e = 50$ mK (see App. C). We note that the rf excitation is continuously

applied for all measurements in this Article.

CHARACTERISING SPIN-ORBIT COUPLING

Having established a method to distinguish between singlet and triplet spin states, our goal is to prepare and coherently control spin states of the DQD through voltage pulses along the detuning axis, ϵ. Such pulses bring the DQD: i) from the (2,0) charge configuration in which a singlet is prepared; ii) into the (1,1) region where the electron spins are spatially separated between QDs and may evolve; and iii) back to an intermediate point where they can be measured (see Fig. 2(a-c). Deep in the (1,1) region, the spin basis states are predominantly $|\uparrow\downarrow\rangle$ and $|\downarrow\uparrow\rangle$. Under an adiabatic ramp to $\epsilon = 0$ for readout, these two states map onto the $|T_0(1,1)\rangle$ and $|S(0,2)\rangle$, respectively. The basis states are separated in energy by $h\Omega = \sqrt{J(\varepsilon)^2 + \Delta E_z^2}$, where we include the kinetic exchange interaction $J(\varepsilon)$ and the Zeeman energy difference between electrons in each dot ΔE_z. The spin detuning $\Delta E_z = \Delta g \mu_B B + g \mu_B \Delta B_{\mathrm{HF}}$ (where μ_B is the Bohr magneton, h is Planck's constant) contains two main contributions: (i) the difference in g-factor be-
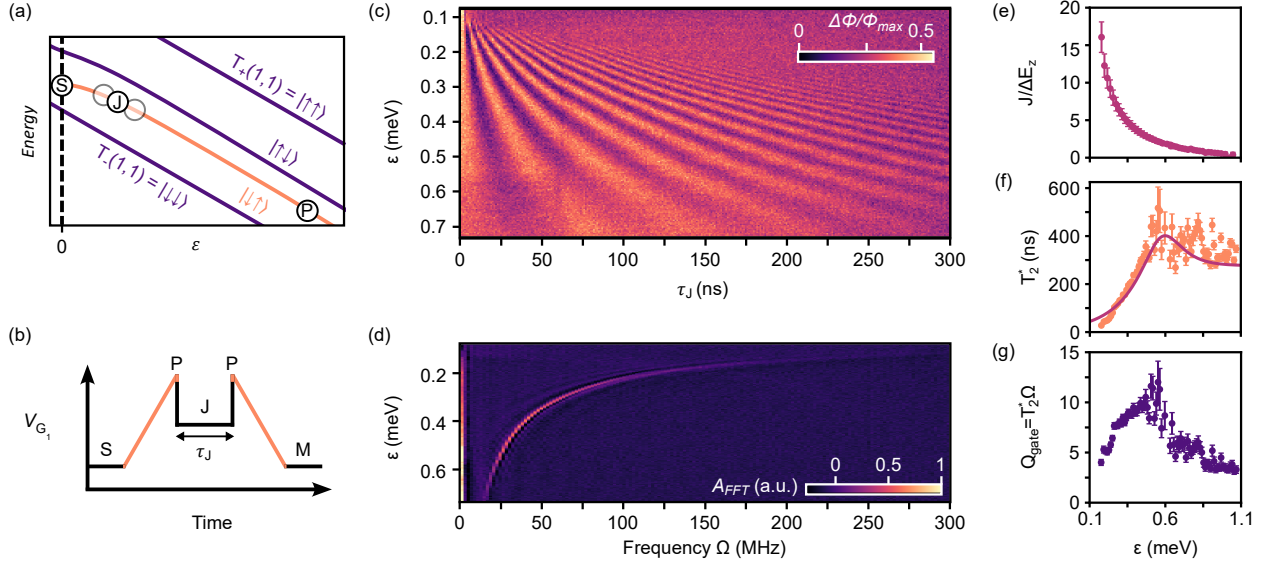
FIG. 3. | **Exchange control in the $^{\mathrm{nat}}$Si double quantum device**. **a**, Energy diagram depicting two-electron spin states in the (1,1) detuning regime, with pulse sequence steps overlaid. **b**, Detuning pulse sequence including initialisation to the $|\downarrow\uparrow\rangle$ state via a semi-adiabatic ramp (orange), followed by a non-adiabatic pulse (J) to near zero-detuning to increase the exchange coupling for duration τ_E. **c**, Exchange driven oscillations between $|\downarrow\uparrow\rangle$ and $|\uparrow\downarrow\rangle$ states, measured rf-phase response proportional to singlet probability, with **d**, the corresponding Fourier transform. **e** Ratio between exchange coupling strength $J(\varepsilon)$ and dot-to-dot Zeeman energy difference ΔE_z. **f** Dephasing time T_2^* extracted from the decay of the exchange oscillations (orange dots) and fit with $T_2^* = \sqrt{\langle(\partial(\hbar\Omega)^2\rangle}/2\hbar$ (purple line) [21, 33]. **g** Gate quality factor.

tween QDs $\Delta g = |g_2 - g_1|$ arising from variations in the spin-orbit interaction (SOI) present near the Si/SiO$_2$ interface [18, 39, 40]; and (ii) the difference in the effective ^{29}Si nuclear magnetic field experienced by each QD, ΔB_{HF}. The random fluctuations in the effective magnetic field experienced by each electron in the DQD can be described by a normal distribution with mean of 0 (given the negligible spin polarisation) and standard deviation $\sigma_{\mathrm{HF}} = 0.13 \pm 0.02$ mT, as we shall see later. This value corresponds to a hyperfine energy strength of 3.4 ± 0.4 neV, which aligns well with other reports in natural silicon [33, 41, 42].

In prior work, the spin detuning ΔE_z has been leveraged to drive oscillations between $|\mathrm{S}\rangle$ and $|\mathrm{T}_0\rangle$ states [18, 42–44]. At an applied magnetic field $B = 250$ mT, we observe similar oscillations using the pulse sequence presented in Fig. 2(a-c): We start in the (0,1) configuration by emptying dot Q_1, then initialise the $|\mathrm{S}(0,2)\rangle$ state via an adiabatic ramp across the (0,1)-(0,2) charge transition. A fast non-adiabatic pulse to ε_P in the (1,1) region leads to oscillations between $|\mathrm{S}\rangle$ and $|\mathrm{T}_0\rangle$ over the course of the dwell time τ_P. The final state is then measured dispersively using a non-adiabatic pulse back to the (1,1)-(0,2) charge transition at $\varepsilon = 0$ for readout. The $|\mathrm{S}\rangle$-$|\mathrm{T}_0\rangle$ oscillations shown in Fig. 2(d) provide a direct measurement of Ω. For $\varepsilon_P \gtrsim 0.9$ meV the dependence of the oscillation frequency on detuning is significantly reduced, suggesting that in this region the ΔE_z term dominates ($J(\epsilon) \leq \Delta E_z$), since Δg is only weakly dependent on detuning ($\partial \Delta g/\partial \varepsilon \approx 0$) [43, 44]. As we shall see

later, at the deepest detuning ($\varepsilon_P = 1.054$ meV), we find $J/\Delta E_z = 0.5 \pm 0.3$.

The strength of the SOI which leads to the Δg term depends on Rashba and Dresselhaus spin-orbit couplings. The SOI (and hence Δg) can be tuned by varying the electrostatic confinement perpendicular to the interface and the transverse magnetic field [18, 39]. We vary the orientation of the in-plane magnetic field and observe changes in the $|\mathrm{S}\rangle$-$|\mathrm{T}_0\rangle$ oscillation frequency, as shown in Fig. 2(e-f). We fit the variation in Ω as a function of the angle, ϕ_B, between the [100] crystal axis and the applied (in-plane) magnetic field [18],

$$\Delta E_z(\phi_B)/h = |B|\,|\Delta\alpha - \Delta\beta\sin(2\phi_B)| + g\mu_B\sigma_{\mathrm{HF}}. \quad (2)$$

The Rashba and Dresselhaus SOI terms are respectively captured by $\Delta\alpha$ and $\Delta\beta$. We find $\Delta\alpha = 5.9^{+1.6}_{-1.5}$ MHz/T and $\Delta\beta = 45^{+5}_{-7}$ MHz/T, which are larger than other reported values [18, 40, 45] and could be partially influenced by the large asymmetry in the gate biasing conditions. The fit assumes that for the fixed detuning of $\varepsilon_P = 0.926$ meV used here, the residual exchange interaction $J(\varepsilon_P)/h = 6.3 \pm 1.9$ MHz is independent of in-plane magnetic field orientation. We operate at an in-plane magnetic field direction near the [1$\bar{1}$0] direction at $\phi_B = 55°$ (235°). Overall, this section expands the recent studies of the SOI in isotopically purified ^{28}Si MOS nanostructures [18, 40, 44, 45] to natural silicon, where the non-negligible effect of the Overhauser field needs to be taken into account.

EXCHANGE CONTROL

We implement exchange control using the sequence depicted in Fig. 3(a,b), where the $|\downarrow\uparrow\rangle$ state is initialised via a ramp from $\varepsilon = 0$ into the (1,1) configuration that is adiabatic with respect to E_z [46]. A fast non-adiabatic pulse towards zero detuning increases the exchange coupling, driving oscillations between the $|\downarrow\uparrow\rangle$ and $|\uparrow\downarrow\rangle$ states at frequency $\Omega(\varepsilon)$, as observed in Fig. 3(c). The final state after some evolution time τ_J is projected to $|S\rangle$ or $|T_0\rangle$ for readout. The Fourier transform of the exchange oscillations (see Fig. 3(d)) reveals a single peak of increasing frequency as the detuning is reduced, indicating the purity of the oscillations and the enhanced exchange strength at lower detuning.

To quantify the properties of these rotations, we combine the results of the exchange oscillations in Fig. 3(c) and the $|S\rangle$-$|T_0\rangle$ oscillations in Fig. 2(d), to extract the ratio $J/\Delta E_z$ and the intrinsic coherence time T_2^* over a wide range of detunings, see Fig. 3(e,f). We extract T_2^* by fitting the oscillations at each detuning point with a Gaussian decay envelope of the form $\exp\left[(-\tau/T_2^*)^2\right]$, and then obtain $\Delta E_z = 9.6 \pm 1.2$ MHz from the fit to the expression

$$\frac{1}{T_{2*}} = \frac{1}{\sqrt{2}\hbar}\sqrt{\left(\frac{J}{h\Omega}\frac{dJ}{d\varepsilon}\delta\varepsilon_{\rm rms}\right)^2 + \left(\frac{\Delta E_z}{h\Omega}\delta\Delta E_{z,{\rm rms}}\right)^2},$$
(3)

where $\delta\varepsilon_{\rm rms}$ and $\delta\Delta E_{z,{\rm rms}}$ refer to the root mean square of the fluctuations in ε and ΔE_z [21, 33, 43].

The extracted $J/\Delta E_z$ ratio is shown in Fig. 3, reducing as a function of increasing ε to a minimum value of 0.5 ± 0.3 at $\varepsilon = 1.054$ meV (beyond this point we cease to observe oscillations). This non-zero minimum shows there remains a residual exchange that cannot be fully turned off, which should be taken into account when designing two-qubit exchange gates.

From the T_2^* data shown in Fig. 3(f), we observe a rapid increase in coherence as the detuning increases from zero, indicative of a low $\delta\varepsilon_{\rm rms}$. The extracted value of $\delta\varepsilon_{rms} = 5.4 \pm 0.1$ μeV, obtained over a measurement time of 79 h, is at the state-of-the-art [18, 21, 33, 43, 47, 48], and can be attributed to the low charge noise achieved for samples using this 300 mm process [10]. As the detuning increases further, where $J < \Delta E_z$, we observe that noise in ΔE_z dominates (due to ^{29}Si nuclear spins), leading to a relatively constant T_2^*. From this saturation value of $T_2^* = 0.28 \pm 0.04$ μs, we extract $\sigma_{\rm HF} = \sqrt{2}\pi\delta\Delta E_{z,{\rm rms}}/(g\mu_B) = 0.13 \pm 0.02$ mT. Note that we assume the Zeeman energy fluctuations are dominated by the Overhauser field rather than noise in the g factor difference.

The entangling two-qubit gate achieved between the spin qubits under the exchange interaction depends on the ratio $J/\Delta E_z$, tending to a $\sqrt{\rm SWAP}$ operation as $J \gg \Delta E_z$ or a C-PHASE when $J \ll \Delta E_z$, though any gate within this set parameterised by $J/\Delta E_z$ can

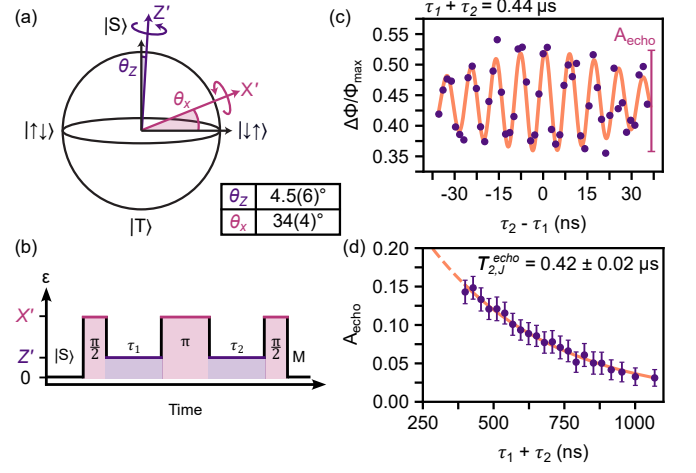FIG. 4. | **Echo sequence**. **a**, Bloch sphere representation of the odd-parity two spin sub-space, indicating the rotation axes, $\hat{Z}'$ and $\hat{X}'$ and their angular deviation from the nominal $\hat{Z}$ axis defined by $|S\rangle$ and $|T_0\rangle$. **b** Schematic of the exchange echo sequence. **c** Echo signal as a function of free evolution time difference $\tau_2 - \tau_1$. **d** Echo amplitude as a function of total free evolution time $\tau_2 = \tau_1$. Data (purple dots) and exponential decay fit (orange line).

be used as the building block for a quantum error correcting code such as the surface code [49]. Defining the gate quality factor as $Q_{\rm gate} = T_2^*\Omega$ (i.e. the number of periods before the amplitude of oscillations decays by $1/e$), we find $Q_{\rm gate} \gtrsim 10$ in the region $J/\Delta E_z = 2.1 - 3.2$. This provides an upper bound estimate on the achievable two-qubit gate fidelity using the approximation $\mathcal{F} \approx 1 - 1/4Q_{\rm gate} \lesssim 98\%$ [50]. To implement error-correctable two-qubit gates this fidelity would need to surpass 99% [1–3], which could be achieved using isotopically enriched silicon. In the next section, we extend the coherence time using spin refocusing techniques.

ECHO SEQUENCE

Dephasing of the two-electron spin state due to low-frequency electric or magnetic noise can be corrected using refocusing pulses. We implement an echo sequence by combining periods of evolution at different detuning points in order to achieve rotations around the two axes, Z' and X' shown in Fig. 4(a). The specific sequence shown in Fig. 4(b), termed the exchange echo, primarily reduces the impact of electric noise [18, 21].

In the exchange echo sequence, after initialising a $|S(1,1)\rangle$ state and applying a $X'_{\pi/2}$ rotation, the two-electron system dephases under the effect of charge noise for a time τ_1. The free evolution occurs at a detuning point where $J/\Delta E_z = 12.8 \pm 1.6$ where we measured $T_2^* = 43 \pm 3$ ns (see Fig 3(f)). We then refocus the spins by applying a X'_π rotation and let the system evolve for τ_2 until a second $X'_{\pi/2}$ rotation maps the resulting state

to the $|\text{S}\rangle$-$|\text{T}_0\rangle$ axis. We extract the amplitude of the echo by fitting the signal in the $\tau_2 - \tau_1$ domain (see Fig. 4(c)), and plot its value as a function of total free evolution time $\tau_1 + \tau_2$. Fig. 4(d) shows the echo amplitude decays exponentially with total time ($\tau_2 + \tau_1$), yielding a characteristic $T_{2,J}^{\text{echo}} = 0.42 \pm 0.02$ μs which corresponds to an order of magnitude increase in the coherence time. From our fit to Eq. (3), we extract a magnetic-noise-limited $T_{2,\Delta E_z}^* = 3.3$ μs at this set point, indicating that sources other than magnetic noise limit $T_{2,J}^{\text{echo}}$. We speculate that residual high frequency charge noise limits the echo coherence [38], and may include factors such as the effect of the rf tone which is on throughout the control sequence.

DISCUSSION

We have demonstrated exchange control, which forms the basis for two-qubit gates between spin qubits, in an MOS DQD device fabricated using a 300 mm wafer process on natural silicon. The quality of the manufacturing manifests in low detuning noise and relatively long T_2^* for natural silicon in a MOS device. These results highlight the benefits of industrial manufacturing and encourage follow-up studies in isotopically enriched Si samples with larger numbers of QDs. Introducing dedicated gates to control primarily the exchange strength over a wider range could be used to (i) enable symmetric exchange pulses and (ii) reduce $J/\Delta E_z$ well below 1, which should lead to an overall reduction in sensitivity to charge noise. Furthermore, the new dispersive readout method demonstrated here using an rf-cascade, expands the portfolio of rf readout methods and provides a solution to the relatively low sensitivity of $in-situ$ dispersive sensing in planar MOS devices. These results may stimulate experiments in which the cascade effect is propagated and readout at a distance which could be achieved by introducing intermediary cascaded QDs. Such an approach would enable enhanced-signal dispersive readout over long distances within dense QD arrays.

METHODS

Fabrication details. The device measured in this study consists of three 30 nm-thick in-situ n^+ phosphorus-doped polycrystalline silicon gate layers formed with a wafer-level electron-beam patterning process. We use a high-resistivity (>3 kΩ/cm) p-type Si wafer. First, a 8 nm-thick, high quality SiO_2 layer is grown thermally to minimize the density of defects in the oxide and at the interface. Then, we subsequently pattern the gate layers using litho-etch processes and electrically isolate them from one another with a 5 nm-thick blocking high-temperature deposited SiO_2 [20]. We employ the first layer of gates (closest to the silicon substrate) to provide in-plane lateral confinement in the direction perpendicular to the double quantum dot axis.

We use the second layer of gates (G_2 in this case) to form and control primarily quantum dot, Q_2. Finally, we use the third gate layer to form and control quantum dot, Q_1, via G_1 and both the multi-electron quantum dot, Q_{ME}, and reservoir via G_S, see Fig. 1(a).

Measurement set-up. We perform the measurements at the base temperature of a dilution refrigerator ($T \sim 10$ mK). We send low-frequency signals through cryogenic low-pass filters with a cut-off frequency of 65 kHz, while we apply pulsed signals through attenuated coaxial lines. Both signals are combined through bias-Ts at the sample PCB (printed circuit-board) level. The PCB was made from RO4003C 0.8 mm thick with an immersion silver finish. For readout, we use radio-frequency reflectometry applied on the ohmic contact of the device. We send radio-frequency signals through attenuated coaxial lines to an on-PCB LC resonator with parallel topology formed by a a coupling capacitor (C_c), a 100 nm-thick NbTi superconducting spiral inductor (L) and the parasitic capacitance to ground (C_p), see Fig. 1(b). We drive the resonator at 512.25 MHz which is the frequency of the system when G_S is well above threshold. The reflected rf signal is then amplified at 4 K and room temperature, followed by quadrature demodulation, from which the amplitude and phase of the reflected signal were obtained (homodyne detection).

DATA AVAILABILITY

The data that support the plots within this paper and other findings of this study are available from the corresponding authors upon reasonable request.

ACKNOWLEDGEMENTS

AUTHOR CONTRIBUTIONS

COMPETING INTERESTS

APPENDIX A: ELECTROSTATIC REQUIREMENTS FOR RF-DRIVEN ELECTRON CASCADE READOUT

The conditions for rf-driven electron cascade are similar to those stated in a previous report on electron cascade with a proximal charge sensor [30]. It can be understood by considering the electrochemical potentials μ_i for each dot Q_i, as well as the given charge configuration $(N_{Q_1}, N_{Q_2}, N_{Q_{ME}})$ where N_{Q_i} refers to the number of charges in dot Q_i, as shown in Fig. 1. For cascade to occur the DQD must be tuned to the $Q_1 - Q_2$ inter-dot charge transition, such that

$$\mu_{Q_1}(1,1,N) = \mu_{Q_2}(0,2,N-1). \tag{4}$$

Note that the opposite inter-dot charge transition $\mu_{Q_1}(2,0,N) = \mu_{Q_2}(1,1,N)$ also satisfies this condition. In addition to this, the reservoir-adjacent dot (Q_{ME}) must be tuned such that

$$\mu_{Q_{ME}}(1,1,N) < 0 < \mu_{Q_{ME}}(0,2,N), \tag{5}$$

where the Fermi level of the reservoir is referenced to 0 and

$$\Delta\mu_{Q_{ME}} = \mu_{Q_{ME}}(0,2,N) - \mu_{Q_{ME}}(1,1,N) \gg 3.5 k_B T, \tag{6}$$

so the shift of the Q_{ME} Coulomb oscillation due to the interdot charge transition is much larger than the Fermi broadening of the reservoir. Here k_B is the Boltzmann constant and T the temperature.

The rf mode of the casacde drive introduces an additional condition that relates to the applied rf modulation amplitude V_{rf},

$$\Delta\mu_{Q_2-Q_1} < eV_{rf} \ll \Delta\mu_{Q_{ME}} \tag{7}$$

where $\Delta\mu_{Q_2-Q_1} = \mu_{Q_2}(1,1,N) - \mu_{Q_1}(0,2,N-1)$. This ensures that the rf modulation only drives tunneling events between Q_1 and Q_2, without directly driving tunneling events between Q_{ME} and the reservoir.

Tuning the quantum dot array into rf-driven electron cascade requires precise control of the electrochemical potentials of the QDs, to the order of 10s of microvolts in the device presented here. The tuning procedure is most clearly demonstrated in the $V_{Q_1} - V_{Q_2}$ gate-voltage-space, as shown in Fig. 5 where in each panel $V_{Q_{ME}}$ is varied, bringing the system into and out of cascade. In this configuration, the range of V_{G_S} bias voltages satisfying the conditions for cascade are given by $V_{G_S}^{casc} = 728.6 \pm 0.1$ mV, a relatively narrow range of voltages as compared to the 14 mV addition voltage of Q_{ME}.

Figure 5 (a) and (e) shows two limiting cases, in which the $\mu_{Q_{ME}}(0,2,N)$ or $\mu_{Q_{ME}}(1,1,N)$ potentials do not meet the condition set by Eq. (4), i.e. the levels are below or above the Fermi level of the reservoir, respectively. Similar cases are observed in panels b and d, where $\mu_{Q_{ME}}(0,2,N)$ or $\mu_{Q_{ME}}(1,1,N)$ now just align with the Fermi level in the reservoir but are within its Fermi broadening. In panel b, the Q_{ME} transition is present in the $(0,2,N\text{-}1) - (0,2,N)$ occupation regime, but absent in the $(1,1,N\text{-}1) - (1,1,N)$ regime. Likewise, in panel d, the Q_{ME} transition is present in the $(1,1,N\text{-}1) - (1,1,N)$ regime but absent in the $(0,2,N\text{-}1) - (0,2,N)$ regime. The contrast in signal between the different charge occupations shown in Fig. 5b and d is well-suited to standard charge sensing. It is only in panel c, when the sequential tunneling event occurs, the cascade conditions are met and we observe the enhanced intensity of the interdot charge transition.

In panels (f-j), we present matching radio-frequency simulations of the triple QD system, see App. D, that highlight the enhanced intensity of the interdot charge transition. Further, we supplement the explanation with schematics of the electrochemical levels in each V_{G_S} conditions in panels k-o.

APPENDIX B: AMPLIFICATION FACTOR

Here, we obtain the expression for the signal amplification factor generated by the cascade process, i.e. Eq. 1 in the main text. To determine the amplification factor, we consider two different charge movement events as seen from the electrode connected to the resonator, in this case, the electron reservoir (R):

1. **In-situ dispersive readout** involving solely a charge transition between Q_1 and Q_2.
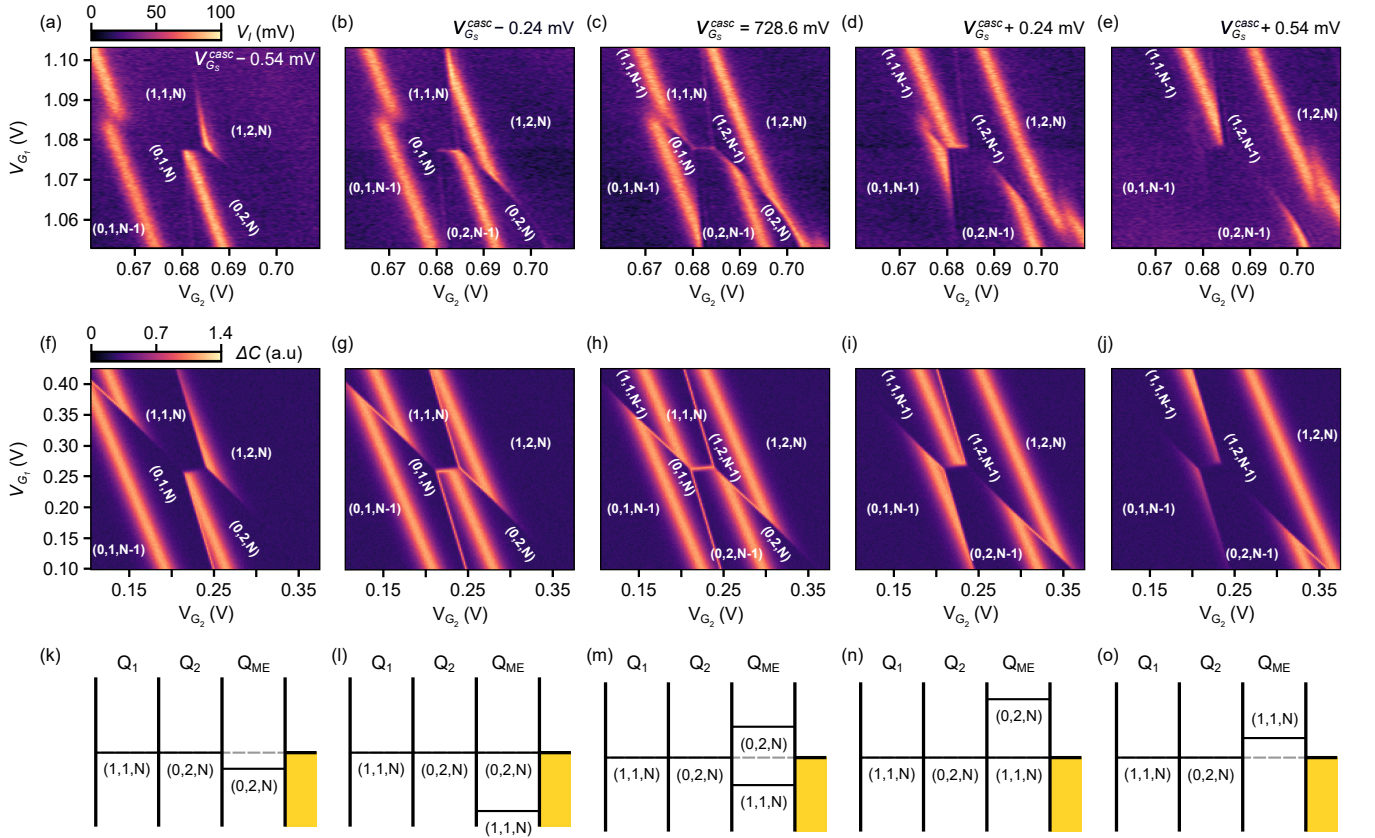
FIG. 5. | **Radio-frequency driven electron cascade**. **a-e**, Charge stability diagrams as a function of the QD gate voltages V_{Gi} for different G_S values refereed as V_{GS}^{casc}. Panel **c** is the bias utilized in the main part of the manuscript. **f-j**, Simulated charge stability diagrams using the methods in App. E. **k-o** Schematic depiction of the electrochemical levels for the corresponding bias conditions, arranged column-wise.

2. **Cascade readout** involving (1) plus the cascaded charge transition between the Q_{ME} and the reservoir.

To obtain the amplification factor, we first consider the expressions of the signal-to-noise ratio (SNR) for case (1) [24]. Particularly, we consider the system is in the low frequency limit $hf_{rf} \ll \Delta_c$ (where f_{rf} is the frequency of the resonator and $\Delta_c = 2t_c$), the small signal regime $Q_L \Delta C_Q/(2C_{tot}) \ll 1$ (where Q_L is the loaded quality factor of the resonator, ΔC_Q is the change in quantum capacitance of the system and C_{tot} the total capacitance of the system) and the large excitation regime, $\alpha_{21} eV_{dev} \gg \Delta_c$ to ensure an electron tunnels every half cycle of the rf excitation. Here $\alpha_{21} = \alpha_{r,2} - \alpha_{r,1}$ is the interdot lever arm as seen from the reservoir and V_{dev} is the amplitude of the oscillatory voltage arriving at the reservoir. In this case, the SNR is

$$\text{SNR}_{21} \propto \frac{(\alpha_{21}e)^2}{k_B T_n} Q_0 Z_r f_{rf}^2 = \frac{I_{R,21}^2 R}{k_B T_n}, \qquad (8)$$

where T_n is the noise temperature of the system, $Q_0 = R\sqrt{C_p/L}$ is the internal quality factor of the resonator, $Z_r = \sqrt{L/C_p}$ is the resonator impedance, R is the resistance (in parallel with L and C_p) representing the losses

in the resonator, and $I_{R,21}$ is the AC current amplitude produced at the reservoir by the oscillatory charge motion between Q_1 and Q_2. Note that $\alpha_{21}ef_{rf} = I_{R,21}$ is the induced current at the reservoir due to the cyclic interdot tunneling.

We now perform the same calculation for the charge transition between the multi-electron quantum dot Q_{ME} and the reservoir R, a dot-to-reservoir transition [26]. Again, considering the small signal regime, the large excitation regime, $\alpha_{ME} eV_{dev} \gg k_B T$ (where α_{ME} is the lever arm from the reservoir to Q_{ME} and T is the electron temperature) and considering additionally the fast tunneling regime $\gamma \gg f_{rf}$ (where γ is the tunnel rate between Q_{ME} and R), we obtain

$$\text{SNR}_{ME} \propto \frac{(1 - \alpha_{ME})^2 e^2}{k_B T_n} Q_0 Z_r f_{rf}^2 = \frac{I_{R,ME}^2 R}{k_B T_n}. \qquad (9)$$

Here, the resonator is coupled the the Q_{ME} via a tunnel barrier, rather than a capacitively coupled gate, and hence the induced charge is $(1 - \alpha_{r,ME})e$.

After this analysis, we highlight a critical result: the SNR is proportional to the square of the AC current amplitude produced by the relevant process, whereas the other two parameters, R and T_n, are independent of the
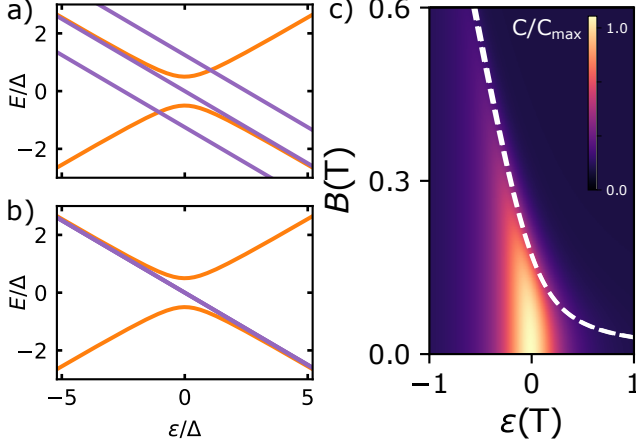
FIG. 6. | **Magnetospectroscopy simulations**. Eigenergies as a fucntion of detuning for $B = 0.5$ T **(a)** and $B = 0$ T **(b)**. Singlets in orange triplets in purple. **(c)** Normalised quantum capacitance versus detuning and magnetic field showing the locatuon of the singlet-triplet minus crossing (dashed white lines).

where $\hat{B} = 2g\mu_{\mathrm{B}}B$, g is the electron g-factor (which we approximate to 2 for both QDs). Then, we calculate the quantum capacitance of the system, C_{Q}, given by,

$$C_{\mathrm{Q}} = -\sum_i (e\alpha)^2 \frac{\partial^2 E_i}{\partial \varepsilon^2} P_i^{\mathrm{th}}. \qquad (14)$$

where E_i are the eigenenergies of the above Hamiltonian and P_i^{th} is the thermal probability of the state i,

$$P_i^{\mathrm{th}} = \exp(-E_i/k_{\mathrm{B}}T_{\mathrm{e}})/Z. \qquad (15)$$

Here, T_{e} is the DQD temperature and Z is the partition function over all states [51]. We plot the results of the simulations in Fig. 6 where, in panel (a) and (b), we show the energy spectrum of the system as a function of detuning for $B = 0.5$ T and 0 T, respectively, and in panel (c), we plot the normalised quantum capacitance of the systems as a function of ε and B. We find that the best match between the data and simulations occurs when $t_{\mathrm{c}} = 2.4$ GHz and $T_{\mathrm{e}} = 50$ mK.

APPENDIX D: CHARGE STABILITY DIAGRAM SIMULATION

To simulate the cascade phenomena we observe in the main text, we calculate the charge stability diagram for a specific voltage configuration using the Constant Inter-action Model [52]. The energies in this model are defined as

$$E = \frac{1}{2}\vec{V}^T \mathbf{C_{cc}^{-1}} \vec{V} \qquad (16)$$

where $\mathbf{C_{cc}}$ is the capacitance matrix for the QDs, containing the mutual capacitance between each pair

$$\mathbf{C_{cc}} = \begin{pmatrix} 24.36 & -3.39 & -1.31 \\ -3.39 & 19.4 & -0.279 \\ -1.31 & -0.279 & 29.2 \end{pmatrix},$$

where each element is given in aF and $\vec{V} = e(\mathbf{C_{cv}}\vec{V_G} - |e|\vec{N})$. Additionally we define $\mathbf{C_{cv}}$ to represent the capacitance matrix governing the interactions between the gate and charges, containing the capacitance between each QD and the corresponding gates,

$$\mathbf{C_{cv}} = \begin{pmatrix} 5.61 & 0.912 & 0.00 \\ 3.356 & 2.83 & 0.00 \\ 0.395 & 0.124 & 12.6 \end{pmatrix}.$$

where each element is given in aF. The number of charges on each dot are given by $\vec{N}$, and $\vec{V_G}$ denotes the applied gate voltages. Throughout the simulations, we use natural units and set the charge of the electron $e = 1$.

Without loss of generality, we assume that an M-quantum dot array can exist in a state from a set of L Fock states, denoted as $\mathcal{F} =$

charge transfer process, particularly in the typical regime where the noise temperature is determined by the first amplifying stage.

With these facts, we arrive to the expression of the amplification factor by considering the two scenarios. In scenario (1), the AC current generated by charge transfer between Q_1 and Q_2 is,

$$I_{\mathrm{R},21} = \alpha_{21}ef_{\mathrm{rf}} = (\alpha_{\mathrm{r},2} - \alpha_{\mathrm{r},1})ef_{\mathrm{rf}}. \qquad (10)$$

In scenario (2), besides the current produced by process (1), we have the current produced by the cascade process adding to a total of,

$$I_{\mathrm{cascade}} \approx I_{\mathrm{R},21} + I_{\mathrm{R,ME}} = (\alpha_{\mathrm{r},2} - \alpha_{\mathrm{r},1})ef_{\mathrm{rf}} + (1 - \alpha_{\mathrm{r,ME}})ef_{\mathrm{rf}}. \qquad (11)$$

We therefore arrive to the expression of the amplification factor A,

$$A = \frac{I_{\mathrm{cascade}}}{I_{\mathrm{R},21}} = 1 + \frac{1 - \alpha_{\mathrm{r,ME}}}{\alpha_{\mathrm{r},2} - \alpha_{\mathrm{r},1}}. \qquad (12)$$

APPENDIX C: MAGNETOSPECTROSCOPY SIMULATION

Here, we describe the simulations of the magnetospectroscopy map in the inset of Fig. 1(c) that allow us to estimate both the tunnel coupling t_{c} and the electron temperature T_{e}. We utilize the simplified Hamiltonian:

$$H = \frac{1}{2}\begin{pmatrix} \varepsilon & \Delta_{\mathrm{c}} & 0 & 0 & 0 \\ \Delta_{\mathrm{c}} & -\varepsilon & 0 & 0 & 0 \\ 0 & 0 & -\varepsilon - \hat{B} & 0 & 0 \\ 0 & 0 & 0 & -\varepsilon & 0 \\ 0 & 0 & 0 & 0 & -\varepsilon + \hat{B} \end{pmatrix}, \qquad (13)$$

$\{\Lambda_j = (\lambda_{1,j}, \ldots, \lambda_{M,j}) \mid \lambda_{i,j} \in \mathbb{Z}^+, \forall j = 1, 2, \ldots, L\}$.
Here $\lambda_{i,j}$ represents the occupancy number of quantum dot i in Fock state Λ_j.

In radio-frequency reflectometry, the measured signal is directly proportional to the change in capacitance of the system, this can be described mathematically as;

$$\Delta C_j = \frac{dQ_T}{dV_j} \qquad (17)$$

Here Q_T denote the total charge of the system and V_j represents the jth gate. We take inspiration from [53] and rewrite the change in capacitance as measured from gate V_j to be;

$$\Delta C_j = \sum_{i=1}^{M} C_{i,j} = e \sum_{i=1}^{M} \alpha_{i,j} \frac{d\langle n_i \rangle}{dV_j} \qquad (18)$$

In this context, $C_{i,j}$ represents the capacitance felt from dot i by gate j. The average occupancy of dot i is denoted $\langle n_i \rangle$. The lever arm matrix is defined as $\hat{\alpha}$ as $\hat{\alpha} = \mathbf{C_{cc}^{-1} C_{cv}}$, which links gate-induced potential changes to the charge states of the quantum dots.

To calculate $\langle n_i \rangle$, we iterate through each Fock state in $\mathcal{F}$ and compute its corresponding probability. Subsequently, a weighted sum of the occupation numbers of each Fock state at position i is performed, as expressed below:

$$\langle n_i \rangle = \sum_{k=1}^{L} \lambda_{i,k} \cdot P_k, \qquad (19)$$

where P_k represents the probability of the quantum dot array being in the Fock state Λ_k.

We assume a Boltzmann distribution and write the probability accordingly;

$$P_k = \frac{1}{Z} \exp\left(-\frac{\epsilon_k}{k_b T}\right) = \frac{\exp\left(-\frac{\epsilon_k}{k_b T}\right)}{\sum_{l=1}^{L} \exp\left(-\frac{\epsilon_l}{k_b T}\right)} \qquad (20)$$

where Z represents the partition function, and ϵ_k represents the energy required for quantum dot array to be in the Fock state Λ_k. Substituting this into equation 19, we obtain;

$$\langle n_i \rangle = \sum_{k=1}^{L} \lambda_{i,k} \cdot \frac{\exp\left(-\frac{\epsilon_k}{k_b T}\right)}{\sum_{l=1}^{L} \exp\left(-\frac{\epsilon_l}{k_b T}\right)} \qquad (21)$$

This term can be further substituted into equation 18, to obtain;

$$\Delta C_{j,\text{tot}} = \sum_{i=1}^{M} C_{i,j} \qquad (22)$$

$$= e \sum_i \alpha_{i,j} \frac{d}{dV_j} \left(\sum_{k=1}^{L} \lambda_{i,k} \cdot \frac{\exp\left(-\frac{\epsilon_k}{k_b T}\right)}{\sum_{l=1}^{L} \exp\left(-\frac{\epsilon_l}{k_b T}\right)} \right) \qquad (23)$$

We use the above formalism to simulate the charge stability diagrams in the $V_{G_1} - V_{G_2}$ gate-voltage space. This can be seen in Fig. 5f-i, where different voltage configurations were applied to the multi-electron dot via V_{G_S}.

[1] A. Noiri, K. Takeda, T. Nakajima, T. Kobayashi, A. Sammak, G. Scappucci, and S. Tarucha, Fast universal quantum gate above the fault-tolerance threshold in silicon, Nature **601**, 338 (2022).

[2] X. Xue, M. Russ, N. Samkharadze, B. Undseth, A. Sammak, G. Scappucci, and L. M. K. Vandersypen, Quantum logic with spin qubits crossing the surface code threshold, Nature **601**, 343 (2022).

[3] M. T. Mądzik, S. Asaad, A. Youssry, B. Joecker, K. M. Rudinger, E. Nielsen, K. C. Young, T. J. Proctor, A. D. Baczewski, A. Laucht, V. Schmitt, F. E. Hudson, K. M. Itoh, A. M. Jakob, B. C. Johnson, D. N. Jamieson, A. S. Dzurak, C. Ferrie, R. Blume-Kohout, and A. Morello, Precision tomography of a three-qubit donor quantum processor in silicon, Nature **601**, 348 (2022).

[4] A. R. Mills, C. R. Guinn, M. J. Gullans, A. J. Sigillito, M. M. Feldman, E. Nielsen, and J. R. Petta, Two-qubit silicon quantum processor with operation fidelity exceeding 99%, Science Advances **8**, eabn5130 (2022).

[5] A. J. Weinstein, M. D. Reed, A. M. Jones, R. W. Andrews, D. Barnes, J. Z. Blumoff, L. E. Euliss, K. Eng,

B. H. Fong, S. D. Ha, D. R. Hulbert, C. A. C. Jackson, M. Jura, T. E. Keating, J. Kerckhoff, A. A. Kiselev, J. Matten, G. Sabbir, A. Smith, J. Wright, M. T. Rakher, T. D. Ladd, and M. G. Borselli, Universal logic with encoded spin qubits in silicon, Nature **615**, 817 (2023).

[6] T. Tanttu, W. H. Lim, J. Y. Huang, N. D. Stuyck, W. Gilbert, R. Y. Su, M. Feng, J. D. Cifuentes, A. E. Seedhouse, S. K. Seritan, C. I. Ostrove, K. M. Rudinger, R. C. C. Leon, W. Huang, C. C. Escott, K. M. Itoh, N. V. Abrosimov, H.-J. Pohl, M. L. W. Thewalt, F. E. Hudson, R. Blume-Kohout, S. D. Bartlett, A. Morello, A. Laucht, C. H. Yang, A. Saraiva, and A. S. Dzurak, Assessment of error variation in high-fidelity two-qubit gates in silicon (2024), arXiv:2303.04090 [quant-ph].

[7] K. Takeda, A. Noiri, T. Nakajima, T. Kobayashi, and S. Tarucha, Quantum error correction with silicon spin qubits, *Nature* **608**, 682 (2022).

[8] S. G. J. Philips, M. T. Mądzik, S. V. Amitonov, S. L. de Snoo, M. Russ, N. Kalhor, C. Volk, W. I. L. Lawrie, D. Brousse, L. Tryputen, B. P. Wuetz, A. Sammak, M. Veldhorst, G. Scappucci, and L. M. K. Vandersypen,

Universal control of a six-qubit quantum processor in silicon, Nature **609**, 919 (2022).

[9] M. F. Gonzalez-Zalba, S. de Franceschi, E. Charbon, T. Meunier, M. Vinet, and A. S. Dzurak, Scaling silicon-based quantum computing using CMOS technology, *Nat. Electron* **4**, 872 (2021).

[10] A. Elsayed, M. Shehata, C. Godfrin, S. Kubicek, S. Massar, Y. Canvel, J. Jussot, G. Simion, M. Mongillo, D. Wan, B. Govoreanu, I. P. Radu, R. Li, P. V. Dorpe, and K. D. Greve, Low charge noise quantum dots with industrial cmos manufacturing, npj Quantum Inf **10**, 70 (2024).

[11] S. J. Pauka, K. Das, R. Kalra, A. Moini, Y. Yang, M. Trainer, A. Bousquet, C. Cantaloube, N. Dick, G. C. Gardner, M. J. Manfra, and D. J. Reilly, A cryogenic cmos chip for generating control signals for multiple qubits, Nat Electron **4**, 64 (2021).

[12] A. Ruffino, T.-Y. Yang, J. Michniewicz, Y. Peng, E. Charbon, and M. F. Gonzalez-Zalba, A cryo-cmos chip that integrates silicon quantum dots and multiplexed dispersive readout electronics, Nat Electron **5**, 53 (2022).

[13] E. Kawakami, P. Scarlino, D. R. Ward, F. R. Braakman, D. E. Savage, M. G. Lagally, M. Friesen, S. N. Coppersmith, M. A. Eriksson, and L. M. K. Vandersypen, Electrical control of a long-lived spin qubit in a si/sige quantum dot, Nat. Nanotechnol. **9**, 666 (2014).

[14] M. Veldhorst, J. C. C. Hwang, C. H. Yang, A. W. Leenstra, B. de Ronde, J. P. Dehollain, J. T. Muhonen, F. E. Hudson, K. M. Itoh, A. Morello, and A. S. Dzurak, An addressable quantum dot qubit with fault-tolerant control-fidelity, Nat. Nanotechnol. **9**, 981 (2014).

[15] S. J. Angus, A. J. Ferguson, A. S. Dzurak, and R. G. Clark, Gate-defined quantum dots in intrinsic silicon, Nano Letters **7**, 2051 (2007).

[16] R. Maurand, X. Jehl, D. Kotekar-Patil, A. Corna, H. Bohuslavskyi, R. Laviéville, L. Hutin, S. Barraud, M. Vinet, M. Sanquer, and S. D. Franceschi, A CMOS silicon spin qubit, *Nat. Commun* **7**, 13575 (2016).

[17] M. Veldhorst, C. H. Yang, J. C. C. Hwang, W. Huang, J. P. Dehollain, J. T. Muhonen, S. Simmons, A. Laucht, F. E. Hudson, K. M. Itoh, A. Morello, and A. S. Dzurak, A two-qubit logic gate in silicon, Nature **526**, 410 (2015).

[18] R. M. Jock, N. T. Jacobson, P. Harvey-Collard, A. M. Mounce, V. Srinivasa, D. R. Ward, J. Anderson, R. Manginell, J. R. Wendt, M. Rudolph, T. Pluym, J. K. Gamble, A. D. Baczewski, W. M. Witzel, and M. S. Carroll, A silicon metal-oxide-semiconductor electron spin-orbit qubit, *Nat. Commun* **9**, 1768 (2018).

[19] A. M. J. Zwerver, T. Krähenmann, T. F. Watson, L. Lampert, H. C. George, R. Pillarisetty, S. A. Bojarski, P. Amin, S. V. Amitonov, J. M. Boter, R. Caudillo, D. Correas-Serrano, J. P. Dehollain, G. Droulers, E. M. Henry, R. Kotlyar, M. Lodari, F. Lüthi, D. J. Michalak, B. K. Mueller, S. Neyens, J. Roberts, N. Samkharadze, G. Zheng, O. K. Zietz, G. Scappucci, M. Veldhorst, L. M. K. Vandersypen, and J. S. Clarke, Qubits made by advanced semiconductor manufacturing, *Nat. Electron* **5**, 184 (2022).

[20] N. I. D. Stuyck, R. Li, C. Godfrin, A. Elsayed, S. Kubicek, J. Jussot, B. T. Chan, F. A. Mohiyaddin, M. Shehata, G. Simion, Y. Canvel, L. Goux, M. Heyns, B. Govoreanu, and I. P. Radu, Uniform spin qubit devices with tunable coupling in an all-silicon 300 mm integrated pro-

cess, in *2021 Symposium on VLSI Circuits* (2021) pp. 1–2.

[21] O. E. Dial, M. D. Shulman, S. P. Harvey, H. Bluhm, V. Umansky, and A. Yacoby, Charge noise spectroscopy using coherent exchange oscillations in a singlet-triplet qubit, Phys. Rev. Lett. **110**, 146804 (2013).

[22] K. Ono, D. G. Austing, Y. Tokura, and S. Tarucha, Current rectification by pauli exclusion in a weakly coupled double quantum dot system, Science **297**, 1313 (2002).

[23] J. M. Elzerman, R. Hanson, L. H. Willems van Beveren, B. Witkamp, L. M. K. Vandersypen, and L. P. Kouwenhoven, Single-shot read-out of an individual electron spin in a quantum dot, Nature **430**, 431 (2004).

[24] F. Vigneau, F. Fedele, A. Chatterjee, D. Reilly, F. Kuemmeth, M. F. Gonzalez-Zalba, E. Laird, and N. Ares, Probing quantum devices with radio-frequency reflectometry, *Applied Physics Reviews* **10**, 021305 (2023).

[25] R. J. Schoelkopf, P. Wahlgren, A. A. Kozhevnikov, P. Delsing, and D. E. Prober, The radio-frequency single-electron transistor (rf-set): A fast and ultrasensitive electrometer, Science **280**, 1238 (1998).

[26] G. A. Oakes, V. N. Ciriano-Tejel, D. F. Wise, M. A. Fogarty, T. Lundberg, C. Lainé, S. Schaal, F. Martins, D. J. Ibberson, L. Hutin, B. Bertrand, N. Stelmashenko, J. W. A. Robinson, L. Ibberson, A. Hashim, I. Siddiqi, A. Lee, M. Vinet, C. G. Smith, J. J. L. Morton, and M. F. Gonzalez-Zalba, Electron cascade for distant spin readout, *Phys. Rev. X* **13**, 011023 (2023).

[27] A. C. Betz, R. Wacquez, M. Vinet, X. Jehl, A. L. Saraiva, M. Sanquer, A. J. Ferguson, and M. F. Gonzalez-Zalba, Dispersively detected pauli spin-blockade in a silicon nanowire field-effect transistor, *Nano Lett* **15**, 4622 (2015).

[28] A. West, B. Hensen, A. Jouan, T. Tanttu, C.-H. Yang, A. Rossi, M. F. Gonzalez-Zalba, F. Hudson, A. Morello, D. J. Reilly, and A. S. Dzurak, Gate-based single-shot readout of spins in silicon, Nat. Nanotechnol. **14**, 437 (2019).

[29] P. Harvey-Collard, B. D'Anjou, M. Rudolph, N. T. Jacobson, J. Dominguez, G. A. Ten Eyck, J. R. Wendt, T. Pluym, M. P. Lilly, W. A. Coish, M. Pioro-Ladrière, and M. S. Carroll, High-fidelity single-shot readout for a spin qubit via an enhanced latching mechanism, *Phys. Rev. X* **8**, 021046 (2018).

[30] C. J. van Diepen, T.-K. Hsiao, U. Mukhopadhyay, C. Reichl, W. Wegscheider, and L. M. K. Vandersypen, Electron cascade for distant spin readout, *Nat. Commun* **12**, 77 (2021).

[31] M. Urdampilleta, D. J. Niegemann, E. Chanrion, B. Jadot, C. Spence, P.-A. Mortemousque, C. Bäuerle, L. Hutin, B. Bertrand, S. Barraud, R. Maurand, M. Sanquer, X. Jehl, S. De Franceschi, M. Vinet, and T. Meunier, Gate-based high fidelity spin readout in a cmos device, Nat. Nanotechnol. **14**, 737 (2019).

[32] D. Gusenkova, M. Spiecker, R. Gebauer, M. Willsch, D. Willsch, F. Valenti, N. Karcher, L. Grünhaupt, I. Takmakov, P. Winkel, D. Rieger, A. V. Ustinov, N. Roch, W. Wernsdorfer, K. Michielsen, O. Sander, and I. M. Pop, Quantum nondemolition dispersive readout of a superconducting artificial atom using large photon numbers, Phys. Rev. Appl. **15**, 064030 (2021).

[33] X. Wu, D. R. Ward, J. R. Prance, D. Kim, J. K. Gamble, R. T. Mohr, Z. Shi, D. E. Savage, M. G. Lagally,

M. Friesen, S. N. Coppersmith, and M. A. Eriksson, Two-axis control of a singlet–triplet qubit with an integrated micromagnet, Proc. Natl. Acad. Sci. U.S.A. **111**, 11938 (2014).

[34] D. J. Niegemann, V. El-Homsy, B. Jadot, M. Nurizzo, B. Cardoso-Paz, E. Chanrion, M. Dartiailh, B. Klemt, V. Thiney, C. Bäuerle, P.-A. Mortemousque, B. Bertrand, H. Niebojewski, M. Vinet, F. Balestro, T. Meunier, and M. Urdampilleta, Parity and singlet-triplet high-fidelity readout in a silicon double quantum dot at 0.5 k, PRX Quantum **3**, 040335 (2022).

[35] M. Hogg, P. Pakkiam, S. K. Gorman, A. V. Timofeev, Y. Chung, G. K. Gulati, M. G. House, and M. Y. Simmons, Single-shot readout of multiple donor electron spins with a gate-based sensor, *PRX Quantum* **4**, 010319 (2023).

[36] G. Zheng, N. Samkharadze, M. L. Noordam, N. Kalhor, D. Brousse, A. Sammak, G. Scappucci, and L. M. K. Vandersypen, Rapid gate-based spin read-out in silicon using an on-chip resonator, Nat. Nanotechnol. **14**, 742 (2019).

[37] T. Nakajima, A. Noiri, J. Yoneda, M. R. Delbecq, P. Stano, T. Otsuka, K. Takeda, S. Amaha, G. Allison, K. Kawasaki, A. Ludwig, A. D. Wieck, D. Loss, and S. Tarucha, Quantum non-demolition measurement of an electron spin qubit, Nat. Nanotechnol. **14**, 555 (2019).

[38] J. Yoneda, K. Takeda, A. Noiri, T. Nakajima, S. Li, J. Kamioka, T. Kodera, and S. Tarucha, Quantum non-demolition readout of an electron spin in silicon, Nat. Commun **11**, 1144 (2020).

[39] M. Veldhorst, R. Ruskov, C. H. Yang, J. C. C. Hwang, F. E. Hudson, M. E. Flatté, C. Tahan, K. M. Itoh, A. Morello, and A. S. Dzurak, Spin-orbit coupling and operation of multivalley spin qubits, Phys. Rev. B **92**, 201401 (2015).

[40] T. Tanttu, B. Hensen, K. W. Chan, C. H. Yang, W. W. Huang, M. Fogarty, F. Hudson, K. Itoh, D. Culcer, A. Laucht, A. Morello, and A. Dzurak, Controlling spin-orbit interactions in silicon quantum dots using magnetic field direction, Phys. Rev. X **9**, 021028 (2019).

[41] B. M. Maune, M. G. Borselli, B. Huang, T. D. Ladd, P. W. Deelman, K. S. Holabird, A. A. Kiselev, I. Alvarado-Rodriguez, R. S. Ross, A. E. Schmitz, M. Sokolich, C. A. Watson, M. F. Gyure, and A. T. Hunter, Coherent singlet-triplet oscillations in a silicon-based double quantum dot, Nature **481**, 344 (2012).

[42] S. D. Liles, D. J. Halverson, Z. Wang, A. Shamim, R. S. Eggli, I. K. Jin, J. Hillier, K. Kumar, I. Vorreiter, M. Rendell, J. H. Huang, C. C. Escott, F. E. Hudson, W. H. Lim, D. Culcer, A. S. Dzurak, and A. R. Hamilton, A singlet-triplet hole-spin qubit in mos silicon

[43] D. Jirovec, A. Hofmann, A. Ballabio, P. M. Mutter, G. Tavani, M. Botifoll, A. Crippa, J. Kukucka, O. Sagi, F. Martins, J. Saez-Mollejo, I. Prieto, M. Borovkov, J. Arbiol, D. Chrastina, G. Isella, and G. Katsaros, A singlet-triplet hole spin qubit in planar Ge, *Nat. Mater.* **20**, 1106 (2021).

[44] R. M. Jock, N. T. Jacobson, M. Rudolph, D. R. Ward, M. S. Carroll, and D. R. Luhman, A silicon singlet–triplet qubit driven by spin-valley coupling, Nat. Commun **13**, 641 (2022).

[45] J. D. Cifuentes, T. Tanttu, W. Gilbert, J. Y. Huang, E. Vahapoglu, R. C. C. Leon, S. Serrano, D. Otter, D. Dunmore, P. Y. Mai, F. Schlattner, M. Feng, K. Itoh, N. Abrosimov, H.-J. Pohl, M. Thewalt, A. Laucht, C. H. Yang, C. C. Escott, W. H. Lim, F. E. Hudson, R. Rahman, A. S. Dzurak, and A. Saraiva, Bounds to electron spin qubit variability for scalable cmos architectures, Nat. Commun **15**, 4299 (2024).

[46] J. R. Petta, A. C. Johnson, J. M. Taylor, E. A. Laird, A. Yacoby, M. D. Lukin, C. M. Marcus, M. P. Hanson, and A. C. Gossard, Coherent manipulation of coupled electron spins in semiconductor quantum dots, Science **309**, 2180 (2005).

[47] Y. He, S. K. Gorman, D. Keith, L. Kranz, J. G. Keizer, and M. Y. Simmons, A two-qubit gate between phosphorus donor electrons in silicon, Nature **571**, 371 (2019).

[48] L. Kranz, S. K. Gorman, B. Thorgrimsson, Y. He, D. Keith, J. G. Keizer, and M. Y. Simmons, Exploiting a single-crystal environment to minimize the charge noise on qubits in silicon, Advanced Materials **32**, 2003361 (2020).

[49] S. M. Patomäki, M. F. Gonzalez-Zalba, M. A. Fogarty, Z. Cai, S. C. Benjamin, and J. J. L. Morton, Pipeline quantum processor architecture for silicon spin qubits, npj Quantum Inf **10**, 31 (2024).

[50] P. Stano and D. Loss, Review of performance metrics of spin qubits in gated semiconducting nanostructures, Nature Reviews Physics **4**, 672 (2022).

[51] T. Lundberg, J. Li, L. Hutin, B. Bertrand, D. J. Ibberson, C.-M. Lee, D. J. Niegemann, M. Urdampilleta, N. Stelmashenko, T. Meunier, J. W. A. Robinson, L. Ibberson, M. Vinet, Y.-M. Niquet, and M. F. Gonzalez-Zalba, Spin quintet in a silicon double quantum dot: Spin blockade and relaxation, Phys. Rev. X **10**, 041010 (2020).

[52] W. G. van der Wiel, S. D. Franceschi, J. M. Elzerman, T. Fujisawa, S. Tarucha, and L. P. Kouwenhoven, Electron transport through double quantum dots, Rev. Mod. Phys. **75**, 1 (2002).

[53] R. Mizuta, R. M. Otxoa, A. C. Betz, and M. F. Gonzalez-Zalba, Quantum and tunneling capacitance in charge and spin qubits, Phys. Rev. B **95**, 045414 (2017).

(2023), arXiv:2310.09722 [cond-mat.mes-hall].